

# Investigation of Multi-Angle Detection Schemes for Light Scattering of Optically Trapped Asymmetric Colloidal Particles

Daniel Maciver<sup>a,\*</sup>, Praveen Parthasarathi<sup>a</sup>, Leo Lue<sup>a</sup>, Jan Sefcik<sup>a</sup>, Mark Haw<sup>a</sup>

<sup>a</sup>*Department of Chemical Engineering, University of Strathclyde, 75 Montrose Street, Glasgow, G1 1XL, Scotland*

---

## Abstract

Optical trapping is a well understood method for transduction and detection of forces on trapped colloidal particles, these trapped entities can be further characterised using light-scattering, posing a two-fold challenge: one experimental, concerning the optimal arrangement of detectors to gather data and minimise signal noise, and the other theoretical, involving solving of the inverse scattering problem in order to interpret light scattering data to determine size, shape, or orientation of the trapped object. Experimentally, combining static light scattering techniques with optical trapping poses significant engineering challenges due to the space constraints in a conventional optical trapping setup. We investigated a plausible scenario of detecting scattered light from an optically trapped asymmetric particles using a novel, multi-angle, optical-fibre based detection scheme, we show how a Bayesian inference-based analysis of the data, combined with a neural-network trained on data simulated to mimic light scattering detection signals in such scenarios, can be used for solving the inverse light scattering problem and characterising colloidal trapped entities. To demonstrate the method, we discuss its application to measuring the instantaneous orientations of a trapped asymmetric microsphere dimer and determine the minimum number of detectors required for a reliable estimation in the presence of signal noise. This approach can be extended to determine any characteristics of the trapped microstructure that influence the light scattering pattern, including size and shape of colloidal objects.

**Keywords:** Optical Trapping, Light Scattering, Measurements, Bayesian Statistics

---

---

\*Corresponding author

Email address: `Daniel.Maciver.2016@uni.strath.ac.uk` (Daniel Maciver)

## 1. Introduction

Since their invention in the late 1980s, optical tweezers have found application in experiments ranging from single molecule biophysics [1] to testing the fundamental assumptions of quantum mechanics [2], thanks to the Brownian dynamics of colloidal systems to the tweezer can transduce and detect forces down to the order of a few pico-newtons. Going beyond forces, further structural, dynamic and chemical characterisation of complex trapped entities could provide useful information, as demonstrated in areas such as metrology [3] and colloidal science [4]. Spectroscopic techniques such as Raman scattering [5] have been used for chemical characterisation of trapped objects, while dynamical characterisation has been demonstrated using data from tweezer’s Quadrant Photo Detector (QPD) by following the centre-of-mass Brownian motion of the trapped entity [6] and measuring rotation of the centre-of-mass [7]. A recent work aimed at characterising trapped entities demonstrated how neural networks can be trained to distinguish between optically trapped microbeads of different size and material by means of a principal component analysis of the forward scattered light detected using a QPD [8]. A more direct, albeit cumbersome attempt at detecting scattered light from trapped biological cells also was attempted [9] where the experimental cuvette was placed inside an elliptical mirror that directed light scattered from the trapped biological-cell onto a photodetector via a rotating aperture that helped select the scattering-angle. Thus, past studies on optical trapping have focused on either on particle trapping to study trapping dynamics, or on the characterisation of particles with relatively simple complex trapping dynamics.

While both [8] and [9] demonstrate some ability to characterise trapped entities, [8] is perhaps best suited to characterise micron-sized particles with simple trapping dynamics, and [9] describes an experimental setup that is difficult to adopt and suffers from a low bandwidth that might not be best suited for monitoring dynamics. A light scattering detection scheme built around an optical trap that is easier to implement and has the advantage of high bandwidth was demonstrated by Safran and co-workers in [10], where a single-mode optical fibre was aligned to detect the scattered light from a trapped bead and study its Brownian motion, commonly now referred to as Localised Dynamic Light Scattering (LDLS). This was later expanded upon [11] by collecting back scattered light to characterise the Stokes friction coefficient as a function of trapping depth. While both papers provided dynamical information, structural information about the trapped bead was not available as the scattered light was only measured across a small angular range. Furthermore, the main drawback to a LDLS is that it cannot be used to characterise asymmetric particles such as dimers or more complex aggregates; in which case the Brownian motion is no longer simply translational, but rotational about the centre of mass [2].

One way of mitigating this is to remove translational fluctuations from the analysis; by monitoring it’s scattering pattern, Cang and co-workers were able to spatially fix a gold nanorod at the centre of trapping laser by moving the sample plane accordingly, to an accuracy of 200 nm [12]. However, this has limited applications to anisotropic scatterers such as biological matter where the internal structure of many cells makes them inherently anisotropic [9]. Thus, even if the Cartesian coordinates are fixed, characterisation of the scattering pattern will have to separate the contributions of size, structure, and orientation. As an example of the relatively sparse literature on measuring orientations of complex trapped objects, [13] employs imaging to study the orientation of trapped dimers: scattering can give more quantitative and potentially more rapid time-resolved information, but only of course if the scattering signals can be interpreted. In this work, we propose a novel approach that expands on the previous approaches [10] [11] to detect scattered light simultaneously at multiple angles (Figure 1), combined with a novel Bayesian inference-based analysis technique, to enable interpretation of the resulting multi-angle data from an anisotropic, asymmetric scatterer, and optimisation to provide maximal information from the detector signals.

To demonstrate this approach, we study an anisotropic scattering entity i.e. an asymmetric dimer, to determine dynamic and structural information about the trapped entity. As a paradigmatic example of extracting information from the scatterer’s scattering data, we explore how to estimate the dimer’s instantaneous orientation from the scattering signals using Bayesian inference, as well as how to optimise the analysis by implementing ‘prior knowledge’ to obtain the most reliable estimate. We, first train a neural network to effectively identify the mapping between scattering signals and dimer orientation, by calculating the scattering signal from a simulated asymmetric dimer undergoing Brownian motion in an optical trap

and mapping to the 2 known instantaneous orientation of the simulated dimer. We then show how Bayesian inference can be used to optimise our estimation of the true dimer orientation from the light scattering signals. Furthermore, we demonstrate how the model's performance when dealing with signal noise, a common problem when analysing scattering behaviour. This approach can be extended to determine any characteristic that influences the light scattering pattern of trapped colloidal objects including: size, shape, and orientation.

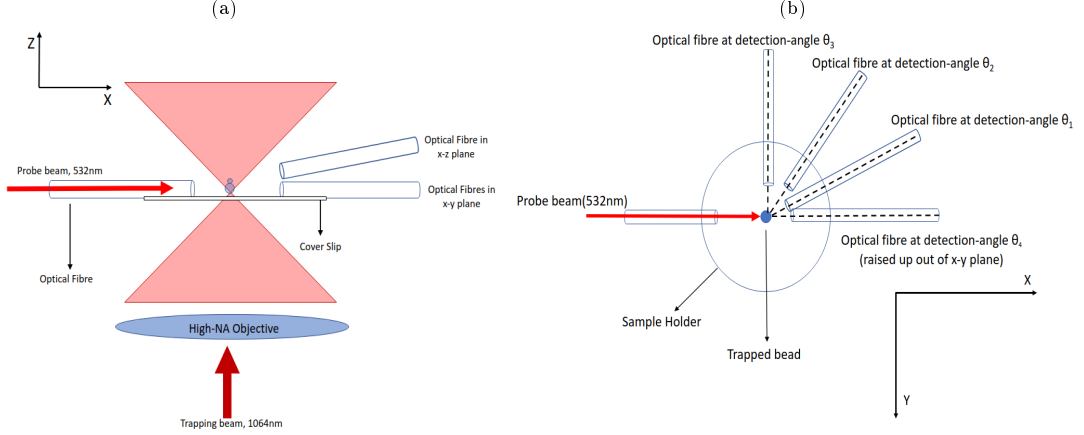


Figure 1: Proposed experimental set up for scattering measurements from an object in an optical trap. The probe beam for scattering measurements is incident perpendicular to the trapping laser propagation direction. a) Side view. b) Top view. Note that three of the detector fibres are co-planar with the incident probe beam, while the fourth detector is placed out of the plane (see Sec 3.1).

## 2. Methodology

### 2.1. Orientation estimation from scattering measurements

Consider a dimer in the optical trap (Fig. 2a), we can define at any point in time a unit vector  $\hat{s}$  pointing from the centre of the larger sphere to the centre of the smaller sphere. A plane wave 'probe' laser, perpendicular to the trapping laser, is incident on the dimer, generating a scattering pattern dependent on the dimer's orientation  $I(\hat{s}, \theta)$  which can be computed using software such as MSTM [14]. To represent the experimental set up consisting of a set of optical fibres recording scattered light, we choose four angles  $(\theta_1, \theta_2, \theta_3, \theta_4)$  and record the calculated intensity at each angle  $\theta_k$ ,  $I(\hat{s}, \theta_k)$ .

Our goal is to determine the orientation of the trapped dimer based on the measured intensity  $I(\hat{n}, \theta_k)$ . Rather than aim immediately for an exact estimate of the dimer's orientation, for the purposes of interpretation of the scattering and optimisation of the measurement setup it is more convenient to discretize the possible orientation space into a number of possible reference orientations, which we can then use as 'classification categories' in a neural network methodology to map scattering data to orientation (see below for further discussion). Here we choose  $n_{ref} = 30$  reference orientations  $\hat{n}_\alpha$  evenly distributed on a unit sphere [15] (Figure 2b) leading to a maximum nearest-neighbour spacing between two neighbouring reference orientations of 0.895 radians. Using MSTM we compute the raw intensities at each of the measurement angles that would be generated by a dimer in each reference orientation,  $I(\hat{n}_\alpha, \theta_k)$ . While the number and position of detection fibres is technically arbitrary there are several constraining factors that limit our ability to infer useful information from the trapped object, see Section 3.1 for a detailed breakdown of our choice of detection angles. The raw intensities are normalized according to:

$$y_k(\hat{n}_\alpha) = \frac{I(\hat{n}_\alpha, \theta_k) - \langle I(\hat{n}, \theta_k) \rangle}{\langle I^2(\hat{n}, \theta_k) \rangle - \langle I(\hat{n}, \theta_k) \rangle^2} \quad (1)$$

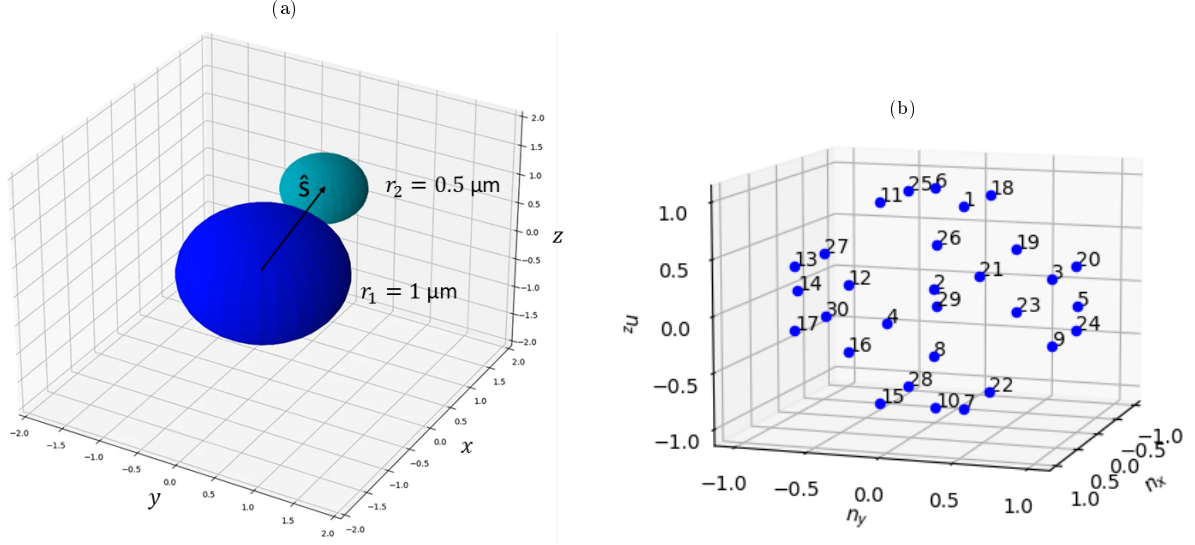


Figure 2: (a) Example dimer in orientation  $\hat{\mathbf{s}}$ , (b) 30 Reference orientations represented by vectors pointing from  $[0,0,0]$  to each point

where the denominator is simply the standard deviation across the set of values  $I(\hat{\mathbf{n}}, \theta_k)$ . The reference orientations, raw intensities, and scaled signals are given in Tables A1 and A2.

Note that the collected scattering signals are not necessarily simply related to their associated reference orientations: as is well known from such examples of the inverse scattering problem. While it is trivial to compute the light scattering pattern for any given particle with any particular characteristic (i.e. size, shape, or orientation), inferring the light scattering from a unknown particle to determine said characteristic is incredibly difficult due to complex mapping between scattering and said characteristic. Even if the orientation space is divided evenly between reference orientation the subsequent signal space ends up being appearing mixed making simple comparisons of signals useless for inferring information on the particle. Shown below is two clusters of orientation vectors and there respective measured scattering signals - the points have been coloured based on their proximity to the centre of their respective cluster. While the orientation space appears tightly packed and ordered the signal space quickly spreads out in an asymmetric fashion. Furthermore as seen in Fig 3b the signal mapping can intersect itself which only further increases the complexity. While in some instances the mapping between one reference orientation and another is discrete, in other instances the mapping becomes far more complex to discern.

Nevertheless, at least where the uncertainty in signal measurements is low (see below), we can predict the orientation from the scattering by utilising computational techniques such as neural networks. We thus utilised the Python machine learning program *scikit-learn* to build a neural network for identifying the dimer's orientation from its light scattering signal. The network was trained by generating a database of random orientation vectors, calculating the corresponding light scattering signals, and then using the network to estimate the probability of a given signal coming from a dimer in a given reference orientation. The network's loss function was evaluated and used to improve the estimation, the network being trained until the improvement in the loss function was less than 0.0001. Importantly, the estimation provided by the neural network can be improved further by accounting for any prior information we know about the dimer, utilising Bayesian inference to update the neural network's estimation:

$$p(\hat{\mathbf{n}}_\alpha | y_k(\hat{\mathbf{s}})) = \frac{p(y_k(\hat{\mathbf{s}}) | \hat{\mathbf{n}}_\alpha) p(\hat{\mathbf{n}}_\alpha)}{p(y_k(\hat{\mathbf{s}}))} \quad (2)$$

where  $p(\hat{\mathbf{n}}_\alpha)$  and  $p(y_1, y_2, y_3)$  are the prior estimates of the distributions of particle orientations and instantaneous

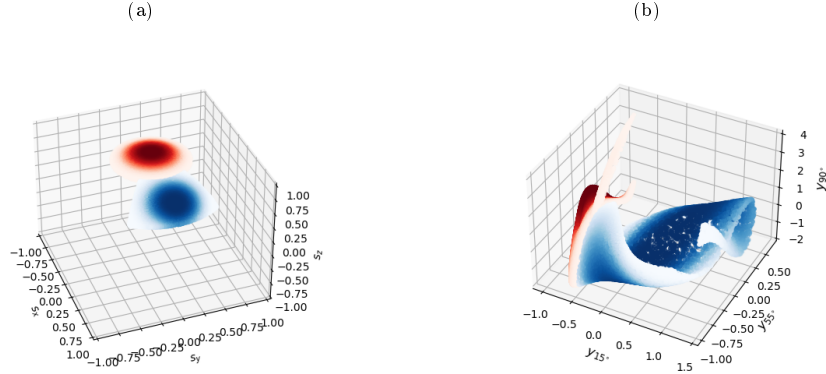


Figure 3: (a) Distribution of orientation vectors and (b) their respective scattering signals. Points are coloured according to their distance from the centre of each cluster (red points centred around  $[0.00, 0.00, 1.00]$ , blue points centred at  $[0.71, 0.00, 0.71]$ )

signals, respectively. *Without* any prior evidence we must assume that the orientation prior of the dimer  $p(\hat{\mathbf{n}}_\alpha)$  is uniform. However, inference about the dimer's possible current orientation from knowledge of previous measurements can be used to inform our estimate of  $p(\hat{\mathbf{n}}_\alpha)$  (see Section 3.2). The latter prior  $p(y)$  is the probability of measuring a signal  $(y_1, y_2, y_3)$ . This is given by taking the discrete integral over the collection of reference orientations:

$$p(y_1, y_2, y_3, y_4) = \sum_{\alpha=1}^{n_{\text{ref}}} p(y_1, y_2, y_3, y_4 | \hat{\mathbf{n}}_\alpha) p(\hat{\mathbf{n}}_\alpha) \quad (3)$$

From (2) we obtain the key result, a mass probability distribution denoting the probability that our dimer is in orientation  $\hat{\mathbf{n}}_\alpha$  given a measured signal  $(y_1, y_2, y_3)$ , *i.e.* an estimated mapping from scattering measurement to orientation estimate.

## 2.2. Calculation of error

To evaluate the above estimation of dimer orientation from scattering signal, we use a Brownian simulation of a dimer in the optical trap (Section 2.3) to compare estimated most probable reference orientation, derived from the dimer's scattering through Eq. (2), with the dimer's known *actual* orientation  $\hat{\mathbf{s}}$ . MSTM provides calculated light scattering from the simulated dimer  $I(\hat{\mathbf{s}}, \theta)$  and we use (1) to obtain normalized values at each measurement angle  $\theta_k$ ,  $y_1(\hat{\mathbf{s}})$ ,  $y_2(\hat{\mathbf{s}})$ ,  $y_3(\hat{\mathbf{s}})$ , from which we obtain  $p(\hat{\mathbf{n}}_\alpha \parallel y_1, y_2, y_3)$ . Because we know the actual orientation  $\hat{\mathbf{s}}$  we can measure the error in the model's estimate by comparing the reference orientation closest to  $\hat{\mathbf{s}}$ , denoted as  $\hat{\mathbf{n}}_{\text{best}}$ , with the most probable predicted orientation from Eq. (2). An ideal result would be one where the probability distribution is 0 for every  $\hat{\mathbf{n}}$  apart from  $\hat{\mathbf{n}}_{\text{best}}$ :

$$p_{\text{best}} = \begin{cases} 1 & \text{when } \hat{\mathbf{n}}_\alpha = \hat{\mathbf{n}}_{\text{best}} \\ 0 & \text{anywhere else} \end{cases} \quad (4)$$

In reality the distribution from Eq. (2) will assign some non-zero probability to every reference orientation, leading to some level 'confidence' in orientation prediction, which can be quantified by calculating the Kullback-Leibler divergence  $K_l$  between the two distributions:

$$K_{l,\#}(p_{\text{best}} \parallel p(\hat{\mathbf{n}}_\alpha | y_1, y_2, y_3)) = p_{\text{best}} \ln \left[ \frac{p_{\text{best}}}{p(\hat{\mathbf{n}}_{\text{best}} | y_1, y_2, y_3)} \right] \quad (5)$$

where a larger value of  $K_l$  indicates that our model is less confident in its prediction of the dimer's orientation. The divergence  $K_l$  thus illustrates the 'spread' in the estimated dimer orientation probability

— a distribution strongly peaked at some value would give us more confidence in that value than a near-uniform distribution where the scattering measurement could imply a wide range of possible orientations — but it does not directly indicate our estimates actual accuracy, that can be simply defined as the percentage of our estimations that are correct.

### 2.3. Brownian Simulation

We use the Brownian OT package developed by Fung *et al* [16] to simulate the motion of an asymmetric dimer (Figure 2a) within an optical trap. Brownian OT combines MSTM [14] and “Optical Tweezer Toolbox” (*ott*) [17] to simulate the motion of arbitrary shaped sphere clusters. We simulate the motion of a dimer trapped in a highly focused Gaussian beam by calculating the optical forces imparted by the laser, and the Brownian force due to the surrounding fluid. MSTM provides the necessary T-matrix to compute the optical force via *ott*. The Brownian force is found by computing the dimer’s diffusion tensor according to the analytical solutions provided by Nir and Acrivos [18]. We simulated a polystyrene dimer ( $n = 1.59$ ) in a suspension of water ( $n_{med} = 1.33$ ) over the course of 1 s with a simulation time step of  $1 \times 10^{-5}$  s. We placed the dimer 4 microns below the trap focus at an angle  $30^\circ$  from the horizontal, the resulting trajectory is shown below in Sec 3.3. We chose these initial parameters because it demonstrates our model’s performance in non steady state conditions.

## 3. Results and Discussion

### 3.1. Minimal number of detectors

The exact number of detectors was initially assumed to be arbitrary, in that it made no difference to our estimate whether we used 2 angles or 200. For practical purposes it seemed beneficial that we demonstrate our method works for a minimal number of detection angles, as geometric constraints come into play when trying to install a high number of detection fibres for any optical tweezer set up.

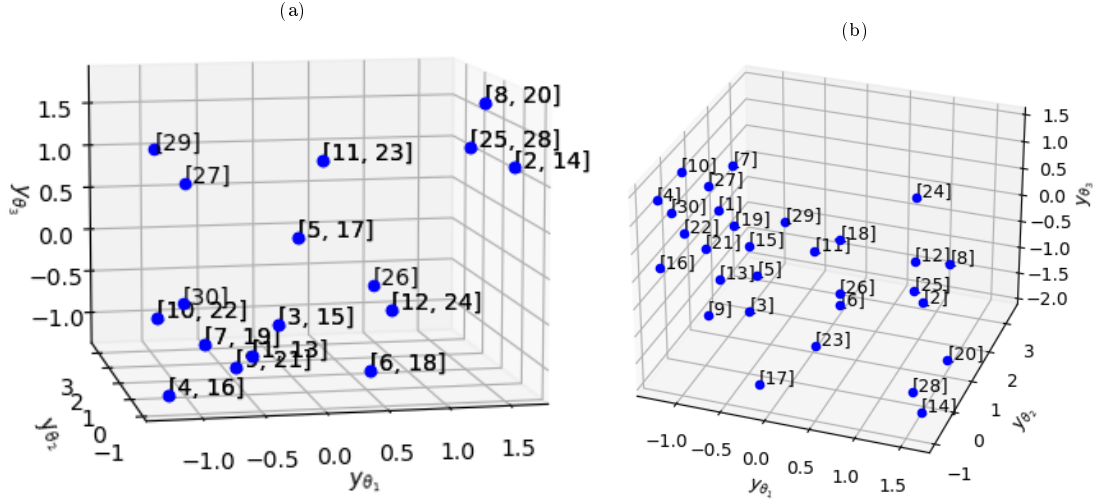


Figure 4: Expected scattered signals from reference orientations -see fig 2 - when: (a) all three detectors are in the X-Y plane, (b) when 1 detector is raised out of the X-Y plane.

When all of the detectors lie in the same plane the expected signal can appear identical despite the dimer being in completely different orientations. This is shown in Figure 4 which plots the expected signals from 30 reference orientations, each point is labelled with its corresponding reference orientation, the fact that points have multiple labels is because the dimer’s scattering is indistinguishable in these two reference orientation. It should be noted that these pairs are reflected in one or more axis which suggests that these are due to the arrangement of our detectors. More specifically, if the detectors are placed say in the x-y

plane then only when the dimer is pointed nearly fully upright will the expected signal be entirely unique. This is illustrative of the difficulty behind the inverse light scattering problem; as one cannot always map a given signal to a particular parameter value.

To remedy this we raise the third detector out of the x-y plane; as such the expected signals from each reference orientation is unique. As seen between Figures 4a & b each reference orientation now has a unique scattering signal, though with only three detectors the difference in expected signals can appear insignificant. By adding a 4<sup>th</sup> detector we can differentiate signals more reliably, improving the neural networks performance. In line with our goal of making this method viable in a laboratory setting we decided not to increase the number of detectors further than 4.

### 3.2. Testing the Model

Using our simulation from Section 2.3 we simulated the motion of a silica dimer ( $n = 1.45$ ) trapped in water ( $n = 1.33$ ) within a 5 mW optical trap. The trapping laser is 1064nm NIR focused through a 1.25 NA objective. The dimer is comprised of two tangent spheres with radii  $1\mu m$  and  $0.5\mu m$  respectively. We simulated the first 10 seconds of motion, calculating the orientation and position every 1 ms.

We applied Eq. (2), taking the reference orientation with the highest probability as our estimate of the dimer's instantaneous orientation  $\hat{\mathbf{n}}_{est}$ . To visualise the model's performance we plotted the radial distance between our estimation  $\hat{\mathbf{n}}_{est}$  and the dimer's *actual* instantaneous orientation  $\hat{\mathbf{s}}$  versus time. For comparison, we also plotted the radian distance between the dimer's instantaneous orientation and the closest reference orientation, denoted  $\hat{\mathbf{n}}_{best}$ . The dotted line indicates the maximum radian distance (0.896 radians) between two *neighbouring* reference orientations: if we are under this line then we know our estimate is at least neighbouring the best result. Assuming a uniform prior of the reference orientations  $p(\hat{\mathbf{n}}_\alpha)$  the neural network's predictions ( $\hat{\mathbf{n}}_{est}$  from Eq. (2)) are at times reasonable, but there are significant large and random jumps away from the correct result (Fig. 5).

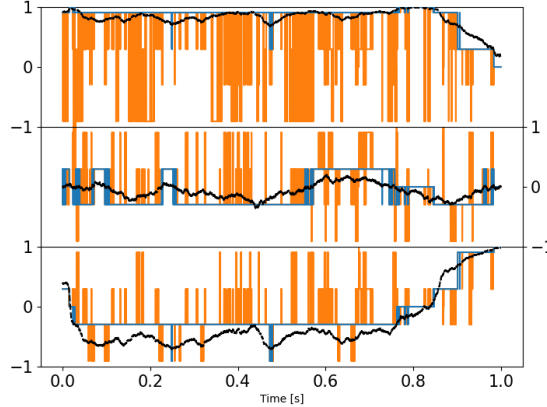


Figure 5: Model's estimation of dimer orientation over the simulation time, assuming uniform prior  $p(\hat{\mathbf{n}}_\alpha)$ , broken up into x, y, and z components for clarity. Blue line denotes the best result we can achieve (the reference orientation  $\hat{\mathbf{n}}_{best}$  that is closest to the actual orientation), orange line denotes the result provided by eq 2: where the orange line is not visible, the model's prediction agrees with  $\hat{\mathbf{n}}_{best}$ . Dotted black line is the instantaneous orientation  $\hat{\mathbf{s}}$ .

One reason we observe such large jumps in orientation estimated from scattering signals is that there is no simple correlation between the 'distance in scattering space' between scattering signals from two different orientations, and their separation in orientation space: even a large change in orientation can involve a small change in scattering. Combining this fact with use of a uniform prior, indicating essentially no knowledge of how orientation should behave, there is no constraint on how much estimated orientation can change from time-step to time-step. To improve the estimation we can therefore use knowledge of the physical limitations of the object in the trap and its dynamics, imposing a more physically grounded prior, accounting in this

case for the fact that the motion of the dimer is limited due to the trap stiffness. Here the prior of the reference orientations  $p(\hat{\mathbf{n}}_\alpha)$  was redefined at each time step as a Boltzmann distribution of the physical distance between the previous estimate  $\hat{\mathbf{n}}_{est}(t - \Delta t)$  and each reference orientation  $\hat{\mathbf{n}}_\alpha$ . Put simply, we are reweighing our estimation based on the size of rotation required, with smaller movements being favoured over large movements:

$$p(\hat{\mathbf{n}}_\alpha) = \frac{e^{\beta(\hat{\mathbf{n}}_\alpha \cdot \hat{\mathbf{n}}_{est}(t-\Delta t))}}{\sum_{\alpha=1}^{n_{ref}} e^{\beta(\hat{\mathbf{n}}_\alpha \cdot \hat{\mathbf{n}}_{est}(t-\Delta t))}} \quad (6)$$

Here  $\beta$  is a weighting factor describing the dimer's freedom of motion within the trap. As shown in Figure 6 implementation of Eq (6) helps significantly reduce the large random excursions of estimated orientation away from the 'best' result.

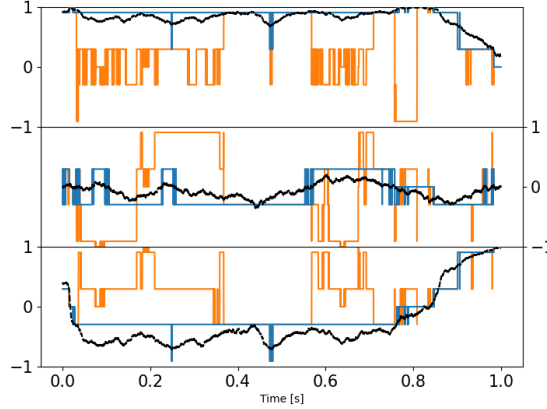


Figure 6: Estimation of dimer orientation with  $p(\hat{\mathbf{n}}_\alpha)$  defined by Eq (6). Blue line denotes the best result we can achieve, orange line denotes the result provided by eq 2. Dotted black line is the instantaneous orientation  $\hat{\mathbf{s}}$  (see Section 2.1).

The simulation data from Section 2.3 was used to evaluate our model's performance — covered in Section 2.2. By summing the divergence of each measurement across the entire simulation we get an evaluation of how well the model performed in estimating the dimer's orientation. To compare the effects of changing certain parameters on the performance of our model we compare our result of  $K_{l,total}$  to a worst case scenario and evaluate how much it improves upon this, denoted as  $F(K_l)$ :

$$K_{l, total} = \sum_{\# = 1}^{timesteps} K_{l, \#} \quad (7)$$

$$K_{l, worst} = \sum_{\# = 1}^{timesteps} \ln \left[ \frac{1}{1/n_{ref}} \right] \quad (8)$$

$$F(K_l) = \frac{K_{l, worst}}{K_{l, total}} \quad (9)$$

The worst case scenario is akin to randomly choosing a reference orientation at each time step. The greater the value of  $F(K_l)$ , the better our model's confidence is in characterising the dimer's motion. Because our model is dependent on several parameters we need to a sophisticated method for understanding how these parameters correlate with  $F(K_l)$ .



### 3.3. Asymmetric dimer dynamics

The Brownian OT software was used to simulate the motion of a trapped dimer ( $a_1 = 1 \mu\text{m}$ ,  $a_2 = 0.5 \mu\text{m}$ ) over the first 1 seconds of entering the optical trap. The initial orientation was set at  $s = (0.923, 0.0, 0.385)$ . The dimer's position and orientation was recorded every  $10 \mu\text{s}$  for using as a test dataset for our model.

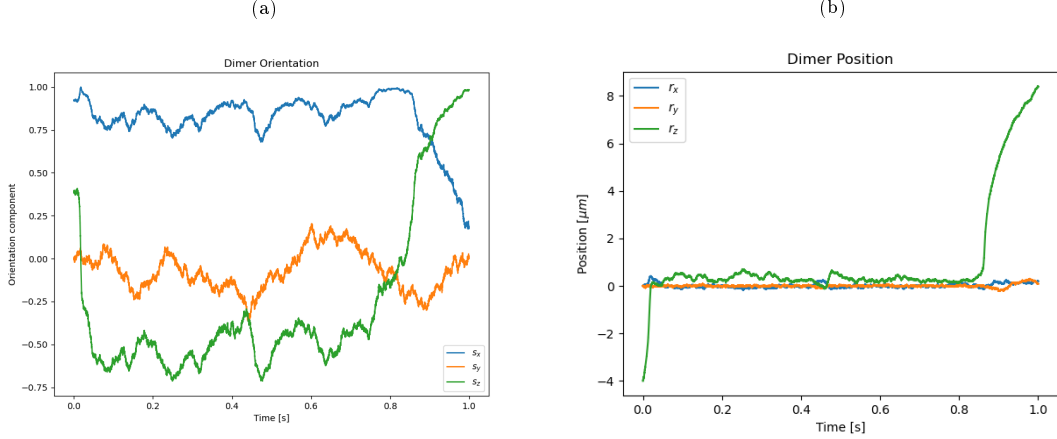


Figure 7: Simulation results of: (a) the dimer's orientation vector with time, (b) the dimer's [x,y,z] position with time.

In the simulations of Vigilante *et al.* [16], trapped symmetrical dimers were investigated; their findings showed that the optical torque on the dimer goes to zero while aligned vertically and is at its maximum in a horizontal alignment. However as seen in Figure 7 asymmetric dimers demonstrate dynamics that do not immediately achieve steady state. We chose to use asymmetric dimers as our benchmark due to this fact, as its orientational motion is far more complex than a symmetric dimer. In the future we hope to further investigate the motion of asymmetric dimers.

### 3.4. Accounting for sources of error in light scattering measurements

When it comes to analysing light scattering from any size particle, error analysis becomes a significant factor. Typically this can be accounted for by averaging over long periods of time to get an assessment of the steady state conditions of the target particle. However in our case where we wish to know the instantaneous orientation, we instead have to rely on our understanding of how uncertainty can effect our model's performance. We identified two areas which are likely sources of error in our estimation: firstly, an incorrect modelling of the target particle, and secondly, signal noise arising from experimental factors. We highlight how we address these areas below.

**Impact of incorrect dimer sizing** One of the main limitations of our model is that we assume that the dimer being modelled in MSTM is accurate to the dimer being trapped in the optical tweezer. Sizing molecules accurately is a significant challenge for single particle analysis so there is bound to be some uncertainty with the measurements. We ran our model 3 times with the neural net being trained on a dimer of size ratio 1 : 1.95, 1 : 2.00 and 1 : 2.05.

As can be seen from Fig 8 even the slightest change in size ratio makes a very significant difference to the performance of our model. This amounts to just over  $100 \text{ nm}$  in the dimer's overall size, yet results in our model being correct from over 90 % of the time to now as low as 30 %. This highlights the importance of correctly sizing trapped entities before performing any in depth analysis of the scattering pattern, as even the slightest deviation can have a serious impact. We addressed this by increasing the number of available reference orientations from 30 to 126 (following the same procedure as given by [15] to evenly space out the coordinates) and increasing the weighting factor in Eq 6. While this didn't have a significant improvement on the overall accuracy of the model, in the worst case having a slight increase from 30.5 % to 40.3 %, it

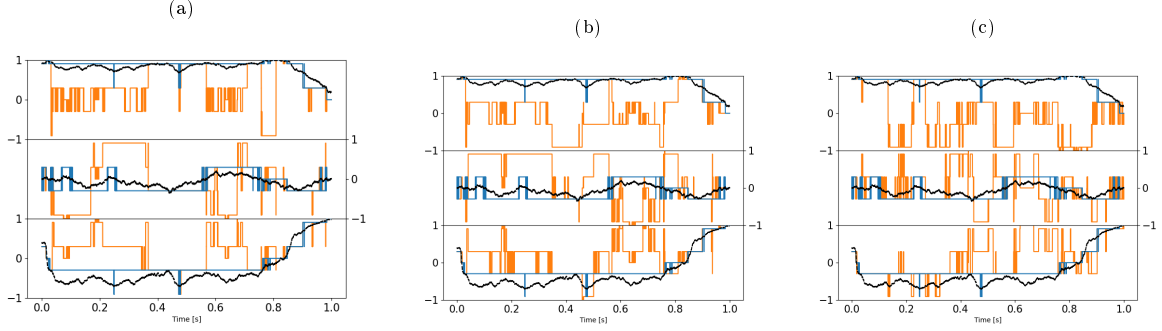


Figure 8: Model estimates of orientation when neural net has been trained on dimer of size ratio: (a) 1:2 [ $F(K_I) = 9.456$ ], (b) 1:2.05 [ $F(K_I) = 1.324$ ], (c) 1:1.95 [ $F(K_I) = 1.325$ ] ( $n_{refs} = 30$ )

did help to significantly reduce the magnitude between our model's estimations and the dimer's motion as seen below in Fig 9.

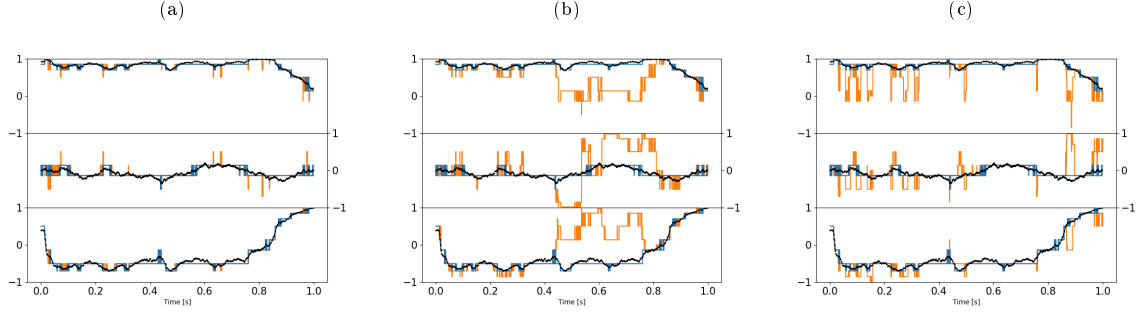


Figure 9: Model estimates of orientation when neural net has been trained on dimer of size ratio: (a) 1:2 [ $F(K_I) = 11.756$ ], (b) 1:2.05 [ $F(K_I) = 1.233$ ], (c) 1:1.95 [ $F(K_I) = 2.128$ ], ( $n_{refs} = 126$ )

Notably the increasing the number of reference orientations had a greater effect when our neural network was trained on a 1:1.95 dimer than a 1:2.05 dimer. This suggests that overshooting our size estimate will be less detrimental to our estimation. Notably if the our sizing is off the neural network does not predict a smooth motion within the trap; instead predicting that the dimer is jumping back and forth between different orientations. This suggest that we can narrow down our estimate of the particle's size by assessing how the dimer is reorienting within the trap, as we should expect a smooth continuous prediction. Since we are working with a spherical dimer it also stands to reason that techniques such as image analysis could be used in part to address this, so long as the trapped entity is sufficiently illuminated.

**Impact of measurement noise on model predictions** So far a key assumption of the neural network implementation is that the detected scattering signal has no uncertainty associated with it. In reality of course scattering signals will always have some non-zero measurement noise. This can be attributed to a variety of factors, from a measurement bias in the detector, to the Brownian motion of the dimer itself. To explore the impact of measurement uncertainty on orientation estimation model performance we introduce a Gaussian noise to the measured signal:

$$I(\hat{\mathbf{s}}) = I(\mathbf{\hat{s}}) \pm \epsilon I(\mathbf{\hat{s}}) \quad (10)$$

where  $\epsilon$  is the percentage error associated with the scattering signal. Figure 10 shows the performance of the model at a range of  $\epsilon$  using in-plane detector angles  $15^\circ$ ,  $55^\circ$ ,  $90^\circ$  and out-of-plane detector at  $75^\circ$ , with  $\beta$  set to 1:

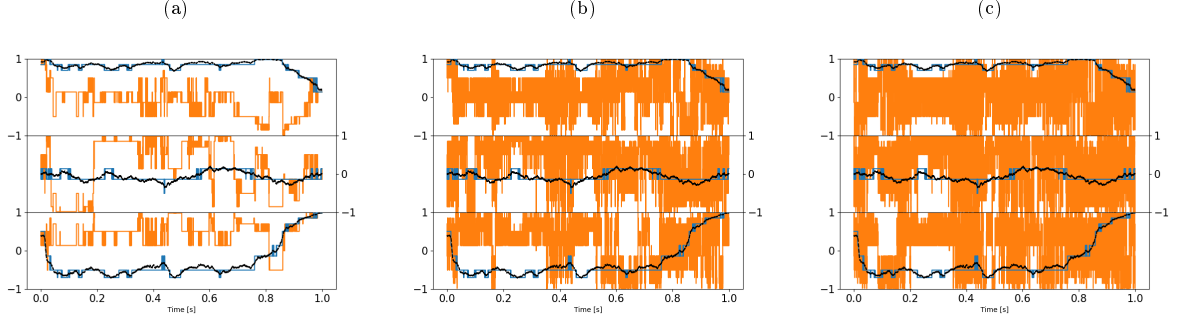


Figure 10: Model prediction for signal error of (a) 1% [ $F(K_I) = 7.246$ ], (b) 15% [ $F(K_I) = 0.511$ ], and (c) 25% [ $F(K_I) = 0.536$ ].

As can be seen from Figure 10, the inclusion of signal noise quickly leads to a decrease in the model's performance. This is due to an inherent feature of the inverse scattering problem: two distinct regions in orientation space can become heavily intertwined and thus no longer well separated when mapped to intensity space (even though the mapping remains continuous): so even small uncertainties in the scattering data can lead to large 'mistakes' in the choice of orientation by the neural network. (Indeed if this was not the case the inverse scattering problem would be quite simple.)

To reduce the effects of the signal noise we took the time average of the expected signal over 0.001s and then had our neural network estimate the orientation based on the average signal.

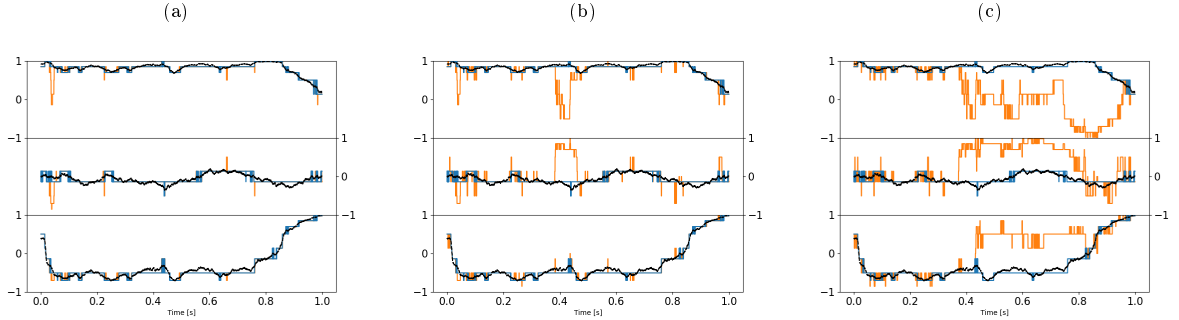


Figure 11: Model prediction for signal error of (a) 1% [ $F(K_I) = 4.823$ ], (b) 15% [ $F(K_I) = 1.494$ ], and (c) 25% [ $F(K_I) = 0.882$ ], time averaged over 1 ms

This resulted in a reduction in the overall signal noise and provided a higher degree of accuracy for our model. There appears to be no clear correlation between the length over which we time average and the performance of our model. Time averaging over every 0.05s resulted in a drastically worse performance; this is due to the fact that over longer time periods there is greater uncertainty regarding how the dimer's orientation has changed, thus tracking the instantaneous orientation becomes harder for the neural network. Fortunately, time averaging even over 1 ms seems to provide a satisfactory estimation of the dimer's angular dynamics within the optical trap.

From the above discussion it's clear that estimation of the dimer's orientation is a problem that can be endlessly tuned to fully maximise our end result. Here we simplify the problem somewhat by employing a relatively small finite number of 'reference orientations' to map between scattering and dimer orientation: the precision of estimation could be improved by utilising a greater number of reference orientations, although there remains a balance between the realisable precision of orientation estimate and the noise level of the scattering measurement. Another avenue to further explore would be using the method to optimise the choice of detection angles, essentially to find the region in the mapping between measured scattering and orientation that offers the best degree of confidence through optimal separation of scattering signals for

distinct orientations. For sequences of data such as dynamic measurements, a further potential enhancement would be to consider more complex correlations based on prior expectations of the dynamics. Here already we improve the method using a non-uniform prior based on only the immediately previous measurement in time (see Section 2.1): considering a non-uniform grouping of reference orientations might result in a better estimation, if we have information regarding the dimer’s preferred axis of rotation.

#### 4. Conclusion

We have developed a method for measuring the dynamics of an optically-trapped colloidal objects based purely on measurements of the object’s light scattering at a small number of detection angles. We demonstrate the method using the orientation of an asymmetric dimer as the dynamic variable and object of interest respectively, but in principle the model can be applied to any characteristic that impacts the light scattering pattern produced by a trapped entity such as size and shape. The MSTM package is a flexible tool for calculating the light scattering of complex objects using a representation of the object as a set of micro-particles, enabling training of a neural network to enable categorisation of the mapping between scattering and trapped object characteristics. By taking account of the physically realistic behaviour of the trapped object and the characteristics of the trap (which impact the dynamics of the object), the Bayesian inference method can be refined to provide a reliable estimation of object characteristics of interest, even in the presence of measurement noise. Fundamentally, the inverse scattering problem is difficult to solve, since the mapping between object characteristics and scattering can be highly complex. We determined the minimum number of detectors required for a reliable estimation in the presence of measurement noise; furthermore, we demonstrated that the arrangement of these detectors is critical for a reliable estimation of an objects orientation. However, Bayesian inference based on neural network estimation of the mapping provides a powerful method for practical applications, extending the use of optical trapping beyond measuring microscopic force response toward detailed structural and dynamic information about complex trapped entities.

**Acknowledgement.** The authors thank the support for this research from the funding provided by the Leverhulme Trust.

**Disclosures.** The authors declare no conflict of interest.

#### References

- [1] C. J. Bustamante, Y. R. Chemla, S. Liu, and M. D. Wang, “Optical tweezers in single-molecule biophysics,” *Nature Reviews Methods Primers*, vol. 1, Mar 2021.
- [2] Z.-q. Yin, T. Li, X. Zhang, and L. Duan, “Large quantum superpositions of a levitated nanodiamond through spin-optomechanical coupling,” *Physical Review A*, vol. 88, no. 3, p. 033614, 2013.
- [3] Y. Arita, S. H. Simpson, P. Zemánek, and K. Dholakia, “Coherent oscillations of a levitated birefringent microsphere in vacuum driven by nonconservative rotation-translation coupling,” *Science advances*, vol. 6, no. 23, p. eaaz9858, 2020.
- [4] M. M. Burns, J.-M. Fournier, and J. A. Golovchenko, “Optical matter: crystallization and binding in intense optical fields,” *Science*, vol. 249, no. 4970, pp. 749–754, 1990.
- [5] P. Gupta and S. Ahlawat, “Raman spectroscopic studies on optically trapped red blood cells,” in *International Conference on Fibre Optics and Photonics*, pp. S3D–2, Optica Publishing Group, 2014.
- [6] L. Friedrich and A. Rohrbach, “Tuning the detection sensitivity: a model for axial backfocal plane interferometric tracking,” *Optics letters*, vol. 37, no. 11, pp. 2109–2111, 2012.
- [7] Y. Yifat, J. Parker, T.-S. Deng, S. K. Gray, S. A. Rice, and N. F. Scherer, “Facile measurement of the rotation of a single optically trapped nanoparticle using the diagonal ratio of a quadrant photodiode,” *ACS Photonics*, vol. 8, no. 11, pp. 3162–3172, 2021.
- [8] I. A. Carvalho, N. A. Silva, C. C. Rosa, L. C. Coelho, and P. A. Jorge, “Particle classification through the analysis of the forward scattered signal in optical tweezers,” *Sensors*, vol. 21, no. 18, p. 6181, 2021.
- [9] D. Watson, N. Hagen, J. Diver, P. Marchand, and M. Chachisvilis, “Elastic light scattering from single cells: orientational dynamics in optical trap,” *Biophysical journal*, vol. 87, no. 2, pp. 1298–1306, 2004.
- [10] R. Bar-Ziv, A. Meller, T. Thursty, E. Moses, J. Stavans, and S. A. Safran, “Localized dynamic light scattering: Probing single particle dynamics at the nanoscale,” *Physical Review Letters*, vol. 78, p. 154–157, Jan 1997.

- [11] N. B. Viana, R. T. S. Freire, and O. N. Mesquita, “Dynamic light scattering from an optically trapped microsphere,” *Phys. Rev. E*, vol. 65, p. 041921, Apr 2002.
- [12] C. Hu, M. W. Chung, X. C. Shan, H. R. Abbas, and Y. Haw, “Confocal three dimensional tracking of a single nanoparticle with concurrent spectroscopic readouts,” *Applied Physics Letters*, vol. 88, 2006.
- [13] A. Raudsepp, G. B. Jameson, and M. A. Williams, “Estimating orientation of optically trapped, near vertical, microsphere dimers using central moments and off-focus imaging,” *Applied Optics*, vol. 61, no. 2, pp. 607–614, 2022.
- [14] D. W. Michael I. Mishchenko, Larry D. Travis, “T-matrix computations of light scattering by nonspherical particles: A review,” *Light scattering by Non-Spherical Particles*, vol. 55, pp. 535–575, 1996.
- [15] G. C. Reythor, *Numerical methods for radiative heattransfer*. Doctoral thesis, Universitat Politècnica de Catalunya, 2006.
- [16] W. Vigilante, O. Lopez, and J. Fung, “Brownian dynamics simulations of sphere clusters in optical tweezers,” *Optics Express*, vol. 28, p. 36131, Nov 2020.
- [17] I. C. D. Lenton, T. A. Nieminen, V. L. Y. Loke, A. B. Stilgoe, Y. Hu, G. Knöner, A. M. Brańczyk, N. R. Heckenberg, and H. Rubinsztein-Dunlop, “Optical tweezers toolbox.” <https://github.com/ilent2/ott>, 2020.
- [18] A. Nir and A. Acrivos, “On the creeping motion of two arbitrary-sized touching spheres in a linear shear field,” *Journal of Fluid Mechanics*, vol. 59, p. 209–223, Jun 1973.

## Appendix

Table A1: Reference Orientations vector components, for  $n_{refs} = 30$  \*

$\alpha$	$\hat{\mathbf{n}}_{\alpha, x}$	$\hat{\mathbf{n}}_{\alpha, y}$	$\hat{\mathbf{n}}_{\alpha, z}$
1	0.2958759	0.2958759	0.9082483
2	0.9082483	0.2958759	0.2958759
3	0.2958759	0.9082483	0.2958759
4	0.2958759	0.2958759	-0.9082483
5	0.9082483	0.2958759	-0.2958759
6	0.2958759	0.9082483	-0.2958759
7	0.2958759	-0.2958759	0.9082483
8	0.9082483	-0.2958759	0.2958759
9	0.2958759	-0.9082483	0.2958759
10	0.2958759	-0.2958759	-0.9082483
11	0.9082483	-0.2958759	-0.2958759
12	0.2958759	-0.9082483	-0.2958759
13	-0.2958759	0.2958759	0.9082483
14	-0.9082483	0.2958759	0.2958759
15	-0.2958759	0.9082483	0.2958759
16	-0.2958759	0.2958759	-0.9082483
17	-0.9082483	0.2958759	-0.2958759
18	-0.2958759	0.9082483	-0.2958759
19	-0.2958759	-0.2958759	0.9082483
20	-0.9082483	-0.2958759	0.2958759
21	-0.2958759	-0.9082483	0.2958759
22	-0.2958759	-0.2958759	-0.9082483
23	-0.9082483	-0.2958759	-0.2958759
24	-0.2958759	-0.9082483	-0.2958759
25	1.000000	0.000000	0.000000
26	0.000000	1.000000	0.000000
27	0.000000	0.000000	1.000000
28	-1.000000	0.000000	0.000000
29	0.000000	-1.000000	0.000000
30	0.000000	0.000000	-1.000000

\*Orientation vector points from centre of sphere 1 to centre of sphere 2.

Table A2: Raw intensities  $I_k^*$  and scaled intensities  $y_k$ 

$\alpha$	$I(\hat{\mathbf{n}}_\alpha, 15^\circ)$	$I(\hat{\mathbf{n}}_\alpha, 55^\circ)$	$I(\hat{\mathbf{n}}_\alpha, 90^\circ)$	$y(\hat{\mathbf{n}}_\alpha, 15^\circ)$	$y(\hat{\mathbf{n}}_\alpha, 55^\circ)$	$y(\hat{\mathbf{n}}_\alpha, 90^\circ)$
1	5.236437793	0.008879799	0.01023413	-0.566323866	-0.895169311	-0.782655503
2	9.029762808	0.014176754	0.023474524	1.604434643	-0.737872411	1.16224444
3	5.677784222	0.018003042	0.012268563	-0.313760083	-0.624248031	-0.48381477
4	4.054681384	0.008596164	0.007681417	-1.242592777	-0.903592052	-1.157627171
5	5.916429873	0.012267124	0.018806686	-0.17719333	-0.794580264	0.47657917
6	7.154962253	0.040816852	0.007678353	0.531566054	0.053224459	-1.158077234
7	4.857371303	0.057897419	0.009575087	-0.78324749	0.560444156	-0.87946335
8	9.018457316	0.061837715	0.027314068	1.597964991	0.677454091	1.726240514
9	5.001594138	0.007138369	0.009576248	-0.700714897	-0.946882332	-0.879292708
10	4.069312021	0.041444603	0.012267124	-1.234220286	0.071865963	-0.484026249
11	6.542222096	0.050631978	0.023474524	0.180920933	0.34469166	1.16224444
12	7.930714067	0.10058846	0.010228239	0.975495811	1.828185342	-0.78352083
13	5.236437793	0.008879799	0.01023413	-0.566323866	-0.895169311	-0.782655503
14	9.029762808	0.014176754	0.023474524	1.604434643	-0.737872411	1.16224444
15	5.677784222	0.018003042	0.012268563	-0.313760083	-0.624248031	-0.48381477
16	4.054681384	0.008596164	0.007681417	-1.242592777	-0.903592052	-1.157627171
17	5.916429873	0.012267124	0.018806686	-0.17719333	-0.794580264	0.47657917
18	7.154962253	0.040816852	0.007678353	0.531566054	0.053224459	-1.158077234
19	4.857371303	0.057897419	0.009575087	-0.78324749	0.560444156	-0.87946335
20	9.018457316	0.061837715	0.027314068	1.597964991	0.677454091	1.726240514
21	5.001594138	0.007138369	0.009576248	-0.700714897	-0.946882332	-0.879292708
22	4.069312021	0.041444603	0.012267124	-1.234220286	0.071865963	-0.484026249
23	6.542222096	0.050631978	0.023474524	0.180920933	0.34469166	1.16224444
24	7.930714067	0.10058846	0.010228239	0.975495811	1.828185342	-0.78352083
25	8.589197415	0.039227387	0.024433841	1.352317814	0.006024147	1.303159911
26	7.179988381	0.037734463	0.014278111	0.545887442	-0.038309302	-0.188629493
27	4.518783843	0.045969647	0.022162922	-0.977006687	0.206240387	0.9695815
28	8.589197415	0.039227387	0.024433841	1.352317814	0.006024147	1.303159911
29	4.635190763	0.153655662	0.02212562	-0.910391959	3.404054059	0.964102078
30	4.290255329	0.010364637	0.014275348	-1.107783832	-0.851075979	-0.189035408

\* $I_k$  values are calculated using MSTM package.